Structure Analysis and Luminescence Properties of Octaethyl(pyrene-tetrakis(biphenyl))tetrakis (phosphonate)

Aysenur Limon, Marcus N. A. Fetzer, Christoph Janiak

crystals

MDPI

Article

Structure Analysis and Luminescence Properties of Octaethyl(pyrene-tetrakis(biphenyl))tetrakis(phosphonate)

Aysenur Limon †, Marcus N. A. Fetzer † and Christoph Janiak *

Institut für Anorganische Chemie und Strukturchemie, Heinrich-Heine-Universität Düsseldorf, D-40204 Düsseldorf, Germany; aysenur.limon@hhu.de (A.L.); fetzer@hhu.de (M.N.A.F.)

* Correspondence: janiak@uni-duesseldorf.de

† These authors contributed equally to this work.

Abstract

We present a modular building block strategy for synthesizing phosphonated polyaromatic systems as an alternative to the conventional late-stage phosphonation of prefabricated aromatic scaffolds, which often requires harsh conditions and has limited tolerance for functional groups. A monophosphonated biphenyl building block was obtained via nickel-catalyzed phosphonation of dibromobiphenyl at 170 °C for three hours. This synthesis is more economical and milder than typical high-temperature palladium systems. In parallel, a borated pyrene derivative was prepared by Suzuki–Miyaura borylation. The final palladium-catalyzed Suzuki cross-coupling reaction produced the target compound, octaethyl(pyrene-tetrakis(biphenyl))tetrakis(phosphonate), Et_8-PyTPPE. Single-crystal X-ray diffraction reveals a centrosymmetric molecule that crystallizes in the triclinic space group P–1, with the inversion center located at the central C–C bond of the pyrene core. The pyrene unit is essentially planar, while the biphenylphosphonate arms are highly twisted relative to the core and to each other. The crystal packing is dominated by weak intermolecular interactions, and no significant π–π stacking is observed. Hirshfeld surface analysis shows that H···H (60.5%) and C···H (22.5%) contacts predominate, while O···H interactions (14.4%) with phosphoryl oxygen atoms represent the most relevant directed contacts. From photophysical investigations, Et_8-PyTPPE exhibits blue fluorescence ($\lambda_{em.}$ = 452 nm) in solution and aggregation-induced red-shifted emission with nanosecond lifetimes in the solid state, confirming purely fluorescent behavior.

Keywords: phosphonate; pyrene; pyrenephosphonate; luminescence; Hirshfeld surface analysis

Academic Editor: Tao Yi

Received: 13 February 2026
Revised: 8 March 2026
Accepted: 10 March 2026
Published: 13 March 2026

1. Introduction

Pyrene has established itself as a versatile building block for functional materials due to its excellent luminescence properties with high fluorescence quantum yields. Its planar structure facilitates π–π stacking interactions, which lead to high charge carrier mobilities and are, therefore, advantageous for thin-film devices [1–5]. Substitution on the pyrene molecule has led to advanced materials that are of great interest in the fields of optoelectronics [6–10], photocatalysis [11–20], and sensor technology [21–25]. Substituted pyrene compounds exhibit interesting properties such as room-temperature phosphorescence [26], temperature-dependent emission [27,28], and mechanochromism [29,30]. Porous photoactive materials, such as MOFs, HOFs, and COFs, are of current interest but have problems in the area of stability [31–38], as they are susceptible to hydrolytic decomposition processes.

In addition, their long-term stability under UV irradiation can be a problem, which is crucial for applications in the fields of photovoltaics and photocatalysis [39–42]. Growing interest in durable and sustainable organic materials, as well as the increasing demand for stable, application-specific, and tailor-made compounds and materials, are driving these areas of research forward.

The introduction of phosphonate groups allows the production of stable organic compounds whose electronic and optical properties can be specifically influenced as required. The simplest synthesis method for phosphonates is the Michaelis–Arbuzov reaction. The P–C and P–O bonds formed through this reaction are thermally and light-stable, as well as hydrolysis-resistant, making them attractive compounds for materials such as sensors, photocatalysts, or organic photovoltaic cells [43–45].

In this context, arylphosphonate compounds are of particular interest for various applications due to their aromatic π systems. The phosphonate groups are capable of forming extremely stable bonds with metallic surfaces. This allows the specific electronic and optical properties of the aromatic systems to be transferred in a targeted manner to application-oriented materials, for example, for use in sensors or organic light-emitting diodes (OLEDs) or organic photovoltaics [46–49].

The attachment of phosphonate groups to pyrene should lead to compounds that exhibit both good luminescence and conductivity through the pyrene core and enable improved stability in the area of porous materials [50,51]. Through catalytic phosphonation of a pyrene core followed by deprotection, the compound pyrene tetraphosphonic acid was synthesized and investigated by Venkatramaiah et al. [52]. This compound and some MOF structures based on it with this deprotonated linker exhibit special properties such as photocatalytic activity or proton conductivity [53–57]. Using p-dimethylphosphonatophenylboronic acid, Schütrumpf et al. were able to synthesize a pyrene tetrakis(phenyl)tetraphosphonate [58].

In this paper, we describe the crystal structure and luminescent properties of the compound octaethyl(pyrene-1,3,6,8-tetrayltetrakis(([1,1′-biphenyl]-4′,4-diyl)))tetrakis(phosphonate) (Et_8-PyTPPE), which we were able to produce in a sustainable three-step organic synthesis (Scheme 1). To the best of our knowledge, Et_8-PyTPPE has not been described in the literature to date.

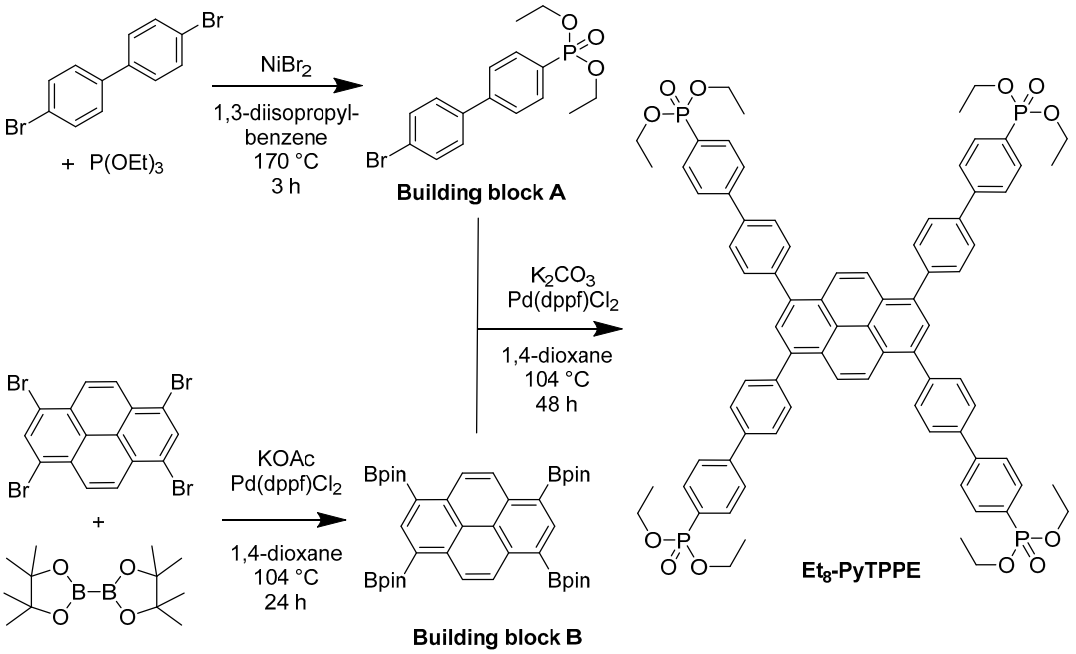

Scheme 1. Synthesis scheme of Et_8-PyTPPE using the two building blocks A and B.

2. Materials and Methods

All chemicals were purchased from commercial suppliers and used without further purification (see Supplementary Material, SM, Section S1 for details). Solvents used in reactions were p. A. grade. Analytical thin-layer chromatography (TLC) was performed on Macherey-Nagel silica gel aluminium plates (Macherey-Nagel GmbH & Co. Kg, Düren, Germany) with F-254 indicator, visualized by irradiation with UV light (λ_{exc} = 254 or 360 nm). Solvents for column chromatography for the preparative purification of synthesis products were technical grade and distilled prior to use. Column chromatography was performed using silica gel Merck 60 (particle size 0.063–0.2 mm, Merck KGaA, Darmstadt, Germany). Solvent mixtures are given as volume/volume ratios. ^{1}H-NMR, ^{13}C-NMR, and ^{31}P-NMR were recorded on a Bruker Avance III 300 MHz NMR spectrometer in $CDCl_3$ (Bruker, Billerica, MA, USA). NMR data are reported as chemical shift (δ) in ppm. ^{1}H-NMR chemical shifts are referenced to the residual proton solvent signal versus TMS (δ($CHCl_3$ = 7.26 ppm). ^{13}C-NMR chemical shifts are referenced to the carbon solvent signal versus TMS (δ($CHCl_3$ = 77.2 ppm). ESI-MS was measured on a Bruker Daltonics UHR-QTOF maXis 4G (Bruker Daltonics GmbH & Co. KG, Bremen, Germany). All MS measurements were completed in positive ion mode. Single-crystal X-ray diffraction data were collected at 150 K on a Rigaku XtaLAB Synergy S diffractometer (Rigaku, Tokyo, Japan) equipped with a PhotonJet Cu Kα radiation source (λ = 1.54184 Å) and a hybrid pixel array detector. Suitable single crystals were selected under a polarized-light Leica M80 microscope (Leica, Wetzlar, Germany) and mounted in oil on a cryo-loop. Data processing, including unit-cell refinement, data reduction, and absorption correction, was carried out with CrysAlisPro 21.5 [59]. Structures were solved and refined in Olex2 using SHELXT and SHELXL, respectively [60–62]. There is a rotational disorder in one of the pendant ethyl groups. The disorder was addressed by splitting the affected atoms over two positions. To ensure a chemically reasonable geometry and stable refinement, two restraints, SADI and SIMU, were applied. Molecular graphics were generated using the Diamond 5 software [63]. Optical measurements were carried out using a reflective setup on an FS5 photoluminescence spectrometer (Edinburgh Instruments, Livingston, UK) equipped with a 450 W Xe arc lamp. For this purpose, the solid sample was placed in a brass sample holder. All measurements were performed in ambient air.

2.1. Synthesis of Diethyl(4′-bromo-[1,1′-biphenyl]-4-yl)phosphonate (Building Block A)

In a two-neck round-bottom flask, 4,4′-dibromo-1,1′-biphenyl (4.0 g, 12.8 mmol) and $NiBr_2$ (600 mg, 2.75 mmol) were suspended in 20 mL of 1,3-diisopropylbenzene under a nitrogen atmosphere. The suspension was heated under stirring to 170 °C. Triethyl phosphite, $P(OEt)_3$ (2.5 mL, 14.6 mmol), was added over a period of 2 h. The reaction mixture was stirred for a further hour at 170 °C, then cooled to room temperature, and excess triethyl phosphite and solvent were removed under reduced pressure. The crude product was purified by column chromatography using ethyl acetate as eluent. The product obtained was a colorless oil, which turned into a colorless solid after one day (yield 2.1 g, 5.68 mmol, 44%). ^{1}H-NMR (300 MHz, $CDCl_3$) δ 7.91–7.83 (m, 2H), 7.66–7.60 (m, 2H), 7.60–7.55 (m, 2H), 7.48–7.44 (m, 2H), 4.25–4.04 (m, 4H), 1.34 (t, J = 7.1 Hz, 6H) (Figure S1).

2.2. Synthesis of 1,3,6,8-Tetrakis(4,4,5,5-tetramethyl-1,3,2-dioxaborolan-2-yl)pyrene (Building Block B)

Under a nitrogen atmosphere, 1,3,6,8-tetrabromopyrene (1.0 g, 1.93 mmol, 1 eq.) and bis(pinacolato)diboron (3.5 g, 13.7 mmol, 7 eq.) were placed in a 100 mL two-neck flask. KOAc (2.0 g, 20.3 mmol, 10 eq.), $Pd(dppf)Cl_2$ (70 mg, 0.09 mmol, 0.05 eq.), and 50 mL of degassed 1,4-dioxane were added to the flask. The reaction mixture was heated to 104 °C

for 24 h. After 24 h, the reaction was cooled to room temperature. To the crude product, 50 mL of ethyl acetate was added, and the organic phase was washed with 50 mL of water and 50 mL of brine. The organic phase was dried of magnesium sulphate, concentrated, and purified by column chromatography using dichloromethane and cyclohexane (5:1 *v*/*v*) as eluent. The resulting product was a pale-yellow powder (yield 980 mg, 72%). ^{1}H-NMR (300 MHz, $CDCl_3$) δ 9.16 (s, 4H), 8.99 (s, 2H), 1.50 (s, 48H) (Figure S2).

2.3. Synthesis of Octaethyl(pyrene-1,3,6,8-tetrayltetrakis(([1,1′-biphenyl]-4′,4-diyl)))tetrakis (phosphonate) (Et_8-PyTPPE)

Under a nitrogen atmosphere, diethyl(4′-bromo-[1,1′-biphenyl]-4-yl)phosphonate (1.25 g, 3.39 mmol, building block A), 1,3,6,8-tetrakis(4,4,5,5-tetramethyl-1,3,2-dioxaborolan-2-yl)pyrene (400 mg, 0.57 mmol, building block B), potassium carbonate (630 mg, 4.56 mmol), and Pd(dppf)Cl_2 (40 mg, 0.05 mmol) were dissolved in 50 mL of degassed 1,4-dioxane. The reaction mixture was heated to 104 °C for 48 h. The reaction mixture was then cooled to room temperature, mixed with 50 mL of ethyl acetate, and washed twice with 50 mL of water. The organic phase was dried over magnesium sulphate and concentrated under reduced pressure. The crude product was purified by column chromatography using a mixture of ethyl acetate and methanol (10:1 *v*/*v*) as eluent. The resulting product was a yellow to orange powder (364 mg, 0.27 mmol, 47%). ^{1}H-NMR (300 MHz, $CDCl_3$) δ 8.29 (s, 4H), 8.12 (s, 3H), 7.98–7.91 (m, 8H), 7.83–7.79 (m, 24H), 4.25–4.10 (m, 16H), 1.37 (t, J = 7.1 Hz, 24H) (Figure S3). ^{13}C-NMR (75 MHz, CDCl3) δ 144.7 (d, J = 3.1 Hz), 140.9, 139.1, 136.9, 132.5 (d, J = 10.3 Hz), 129.5, 129.2 (d, J = 315.7 Hz), 128.5, 128.4, 127.4 (d, J = 4.3 Hz), 127.1, 126.1, 126.0, 125.6, 62.3 (d, J = 5.4 Hz), 16.5 (d, J = 6.5 Hz) (Figure S4). ^{31}P-NMR (121 MHz, $CDCl_3$) δ 18.8 (s) (Figure S5). MALDI-TOF MS: $[M]^+$ 1354.68 (Figure S6). HR-ESI-MS: obs. 678.2307, calc. 678.2295 $[M+2H]^{2+}$ (Figure S7).

3. Results and Discussion

3.1. Synthesis

The classical approach to the synthesis of phosphonated aromatic compounds is usually based on the successive construction of the aromatic skeleton, followed by late functionalization through halogenation and subsequent phosphonation (Supplementary Materials, Scheme S1). Although this approach is widely used, it is often associated with significant synthetic limitations. In particular, problems arise with regard to the targeted functionalization of complex molecules and the tolerance of different functional groups to the harsh conditions of phosphonation [64–67]. These difficult synthetic requirements significantly limit the reproducibility and scalability of the syntheses. Against this background, the present work pursued a modular synthesis approach based on the targeted preparation of two independent functionalized building blocks (Scheme 1). This strategy allows the individual functionalization steps to be decoupled from each other and the building blocks to be selectively combined into the target molecule in a final coupling reaction. The two central synthesis steps comprise a C–P bond formation (phosphonation, building block A, Scheme 1) and a C–B bond formation (boration, building block B, Scheme 1). Dibromobiphenyl was used as the starting compound for the phosphonation. According to the literature, aromatic phosphonations to form C–P bonds usually require high reaction temperatures and the use of transition metal catalysts. Temperatures between 160 and 250 °C are standard. Palladium or nickel catalysts are often used for this purpose, often with high loadings of expensive palladium catalysts and temperatures above 200 °C, with reaction times ranging from several hours to several days [68–70]. To the contrary, this work was able to achieve a more economical and, at the same time, milder reaction with nickel bromide as a catalyst. Under these conditions, the desired monophosphonated

biphenyl was obtained after only 3 h of reaction time at 170 °C (Scheme 1, building block A). The moderate yield of 44% is due to the partial further reaction to diphosphonated biphenyl, so that the isolated product can be regarded as a reactive intermediate within the phosphonation sequence.

In parallel, a Suzuki–Miyaura borylation was carried out, in which 1,3,6,8-tetrabromopyrene was reacted with bis(pinacolato)diboron (B_2pin_2) (Scheme 1, building block B). The resulting boronated pyrene derivative, which is also commercially available, acts as the second key building block in the synthesis route presented here and allows efficient further functionalization of the pyrene core. The final assembly of the two building blocks was then carried out via a palladium-catalyzed Suzuki cross-coupling, which led to the successful formation of the target molecule Et_8-PyTPPE in the form of a yellow solid (Figure S18a). In addition to the NMR and MS analyses (Figures S3–S7), we were able to crystallize the product Et_8-PyTPPE from chloroform and n-hexane. Single-crystal X-ray structural determination confirms the molecular constitution (Figure 1).

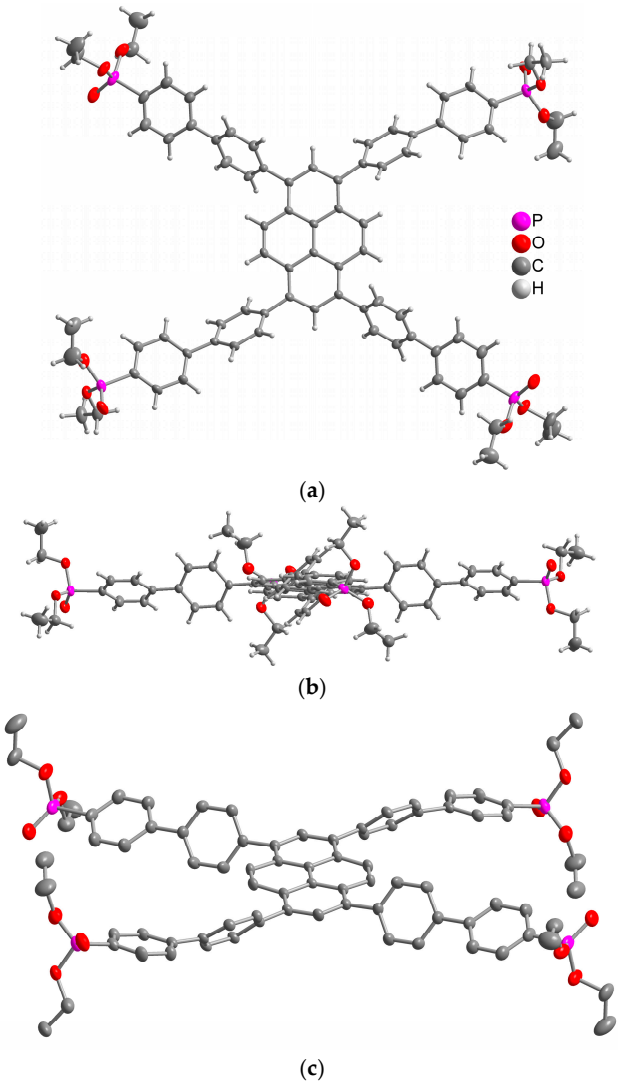

Figure 1. Molecular structure of Et_8-PyTPPE in the crystal (50% thermal ellipsoids; H atoms with arbitrary radii). A disorder in the ethyl groups is shown in the Supplementary Materials for clarity. For the disorder and a figure with atom labeling, see Figure S8, Section S4; (**a**) view approximately perpendicular to the pyrene core; (**b**) view parallel to the pyrene core to better visualize the dihedral angles and the up-and-down orientation of the ethoxy groups on the phosphonate groups (see Table S2 for dihedral angles); (**c**) perspective view of the structure without hydrogen atoms.

A comparison of the synthesis route presented here with that of Schütrumpf et al. highlights the advantages of the building block-based approach which we used [58]. The targeted combination of two functionalized reaction partners, each carrying a crucial functional group (building block A = phosphonate, building block B = boronate) for the final coupling, can, in future work, open up access to a significantly expanded structural diversity. The biphenyl bromophosphonated intermediate (building block A) synthesized in this work is not limited to Suzuki coupling but is also suitable in principle for other transition metal-catalyzed cross-couplings such as the Stille, Negishi, or Kumada reactions. Conversely, the use of boronated pyrene derivatives enables the attachment of a wide variety of phosphonated halogenated aromatics to the pyrene core, making a multitude of differently substituted pyrene structures accessible.

In addition to the expanded structural diversity, the synthesis strategy that we presented offers another decisive advantage in terms of occupational safety and sustainability. While Schütrumpf et al. use highly toxic organic tin compounds in combination with the radical initiator azobisisobutyronitrile (AIBN) for the synthesis of p-dimethylphosphonatophenylboronic acid [58], this hazard could be completely avoided in the present work. The functional separation into two independent building blocks opens up a synthetically flexible and, at the same time, toxicologically less problematic route, which is particularly advantageous for future scaling and material chemistry applications.

3.2. Crystal Structure

The compound Et_8-PyTPPE crystallizes in the centrosymmetric triclinic space group P-1, and the midpoint of the central C-C bond of the pyrene core coincides with the inversion center in this space group. Thus, the asymmetric unit consists of only half the molecule, and the opposite [1,1′-biphenyl]-4′,4-diylphosphonate arms are related by symmetry (Figure S8). The pyrene core is essentially planar, with the largest deviations from the average ring plane of 0.072(4) Å and 0.065(4) Å for the two carbon atoms that bind the biphenylphosphonate groups. The biphenyl ring planes are tilted with respect to the pyrene core and toward each other (Figure 1b). Interplanar angles are 60.0(2)° and 44.7(2)° for the phenyl-pyrene ring planes and 38.3(2)° and 42.9(2)° for the biphenyl ring planes in the two symmetry-independent [1,1′-biphenyl]-4′,4-diylphosphonate arms (see Table S2 for specific angle assignments). One pendant ethyl group of the asymmetric unit was found to be disordered over two positions (Figure S8, Section S4). The disorder was refined using a split-atom model to maintain a reasonable geometry.

There are no significant π–π stacking and only weak C–H···π interactions between the Et_8-PyTPPE molecules. Relevant π–π stacking interactions require centroid–centroid contacts of less than 3.8 Å, near-parallel ring planes, small slip angles, and small vertical displacements (slippage < 1.5 Å), which would translate into a sizable overlap of the aryl-plane areas [71,72]. In the packing of Et_8-PyTPPE, the shortest centroid–centroid contact is 3.97 Å (ring C21-C26 to C21-C26 with symmetry relation 1-x, 1-y, 1-z) with parallel ring planes but large slip angles and a large slippage of 1.95 Å. Significant intermolecular C-H··· π contacts are below 2.7 Å for the (C-)H···ring centroid distances, with H-perp also below 2.6–2.7 Å and C-H·· centroid > 145° [73,74]. In the structure of Et_8-PyTPPE, the shortest (C-)H···ring centroid distance is 2.79 Å with H-perp 2.71 Å and C-H·· centroid 146° (Table S3, Figures S10 and S11). A void analysis performed with Mercury [75] (probe radius of 1.2 Å) yielded a total void volume of approximately 15 $Å^3$ or 0.9% of empty space per unit cell volume; hence, the molecules are closely packed, leaving no solvent accessible void volume.

To place our structure into a broader crystallographic context, a comparative analysis with related tetra-phosphonate aromatic systems from the Cambridge Structural Database

(CSD) was performed. The P=O (1.46 Å) and P–O (1.57–1.59 Å) bond distances are in excellent agreement with reported values for similar architectures. Specifically, comparisons were made with the structures reported by Venkatramaiah et al. (Ref.-Code: OCAQER, CCDC 1012817) and Zheng et al. (Ref.-Code: BARLIS, CCDC 1450122) [76,77]. These references also highlight positional disorder within the ethyl groups of the ester and also larger R1 and wR2 values. Consistent with these references, the structural flexibility in our compound may be a characteristic trait of bulky octaethyl phosphonate architectures rather than an experimental artifact.

3.3. Full Interaction Map (FIM)

To analyze the Et_8-PyTPPE molecule further in terms of its possible interactions with other molecules, a Full Interaction Map analysis (FIM) was employed using the program Mercury [75] to visualize the interaction preferences of the molecule as presented in Figure 2. The FIM analysis is based on the Cambridge Structural Database (CSD) and, therefore, employs a predictive model based on experimental data, which provides a deeper insight into which positions on Et_8-PyTPPE other molecules would dock to with their groups.

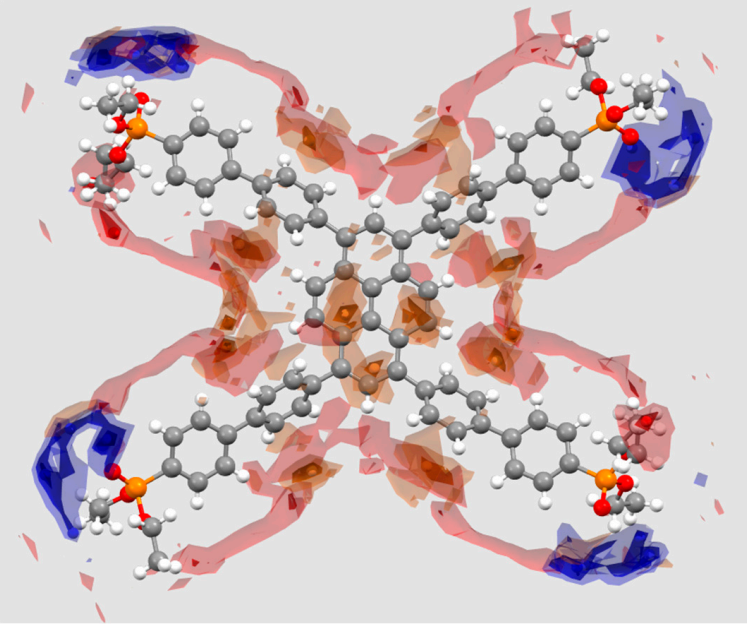

Figure 2. Full Interaction Map (FIM) of Et_8-PyTPPE calculated using the program Mercury. The map was generated with default probe settings (uncharged NH nitrogen, carbonyl oxygen, and aromatic CH carbon). Colored isosurfaces indicate the areas for uncharged amino groups as hydrogen bond donors (blue) and carbonyl oxygen as hydrogen bond acceptors (red) to interact with Et_8-PyTPPE and for aromatic CH carbon to enter into hydrophobic interactions (brown) with Et_8-PyTPPE.

The blue isosurfaces, representing the probability for hydrogen bond donor positioning, are concentrated around the electron-rich phosphoryl oxygen atoms. This highlights the propensity of the oxygen atoms to serve as hydrogen bond acceptors. Conversely, the red isosurfaces show the preferred regions for hydrogen bond acceptors. These regions indicate the ethyl and aromatic C–H groups as weak hydrogen bond donors. Finally, the brown isosurfaces indicate regions favorable for hydrophobic interactions. As illustrated in Figure 2, the latter surfaces are pronounced around the pyrene core, highlighting a probability of van der Waals interactions or π–π stacking within the crystal lattice.

3.4. Hirshfeld Analysis

Hirshfeld surface analysis and corresponding fingerprint plots were generated to visualize intermolecular interactions using the CrystalExplorer 17 [78] software to provide a detailed statistical breakdown of the interaction landscape that goes beyond qualitative observation. Furthermore, the 2D-fingerprint plots allow a precise analysis of the molecular surface, quantifying the relative percentile contributions of specific contact types. The strength of the interactions was evaluated using the normalized contact distance (d_{norm}), which compares the distances to the nearest internal (d_i) and external (d_e) atoms with their respective van der Waals radii [79,80]. This mapping highlights regions of significant intermolecular contacts that are less than the sum of the van der Waals radii, visualized as red regions on the surface, while contacts longer than the sum are colored in blue [81].

The 3D Hirshfeld surface analysis of the compound in Figure 3 reveals characteristic red spots around aromatic C–H atoms and the P–O group, indicating intermolecular contacts.

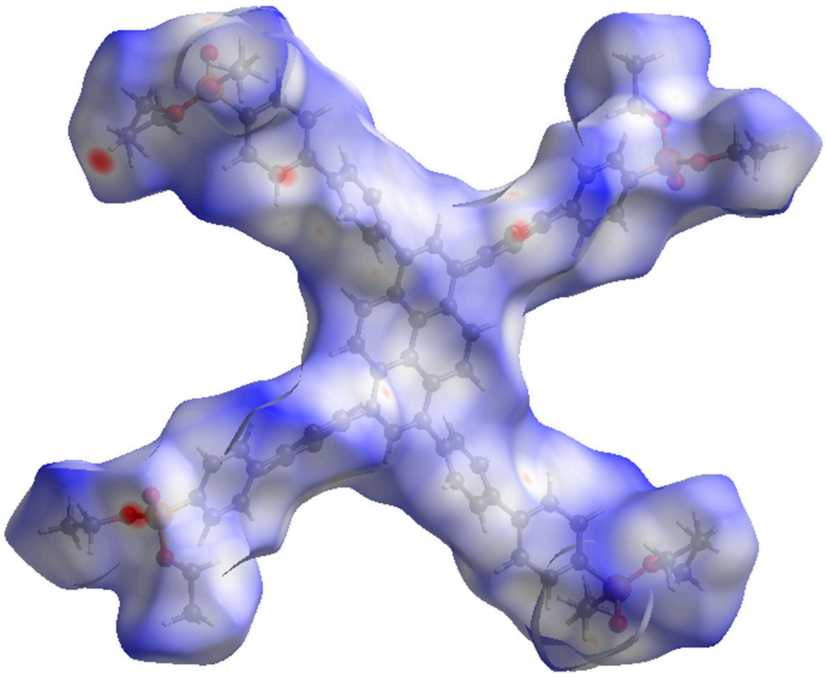

Figure 3. Three-dimensional Hirshfeld surface representation of Et_8-PyTPPE plotted over d_{norm}. ($d_{norm} < 0$, red regions, indicating strong attractive interactions to an adjacent molecule; $d_{norm} > 0$, blue regions, indicating interactions weaker than the van der Waals interactions).

Intermolecular contacts were further visualized using 2D Hirshfeld fingerprint plots, represented as a mapping of d_e against d_i (Figures 4 and S12–S15). The fingerprint plot exhibits characteristic spikes directed toward the lower-left corner, which are indicative of P–O···H bonds (see also Figure S12). Quantitative analysis reveals that these spikes extend to approximately (d_i, d_e) ≈ (0.9, 1.4) Å and correspond to O···H contacts. These interactions represent a significant contribution to the molecular packing, accounting for 14.4% of the total Hirshfeld surface area. To further delineate the individual contributions, individual sub-plots for O···H, C···H, H···H, and C···C interactions are provided in the Supplementary Materials, Section S5 as Figures S12–S15. The remaining 85.6% of the surface is dominated by weaker van der Waals forces: H···H contacts constitute the largest fraction at 60.5% (Figure S13), followed by C···H interactions at 22.5% (Figure S15), whereas C···C interactions contribute only marginally at 2.7% (Figure S15).

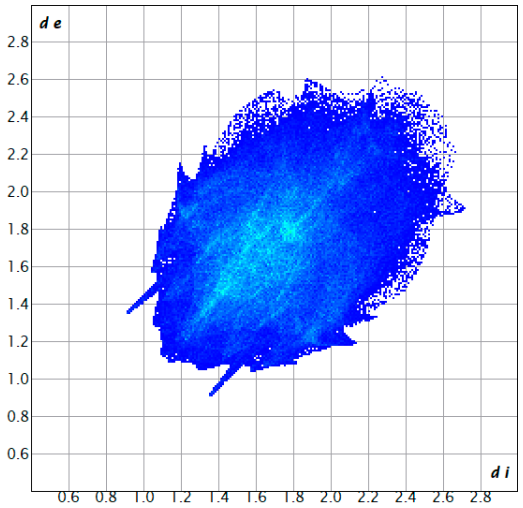

contact	contribution
O···H	14.4
C···H	22.5
H···H	60.5
C···C	2.7

Figure 4. Two-dimensional fingerprint plot and contribution of the specific non-covalent atomic contacts (O···H, C···H, H···H, and C···C) to the Hirshfeld surface of Et_8-PyTPPE. The spikes represent the shortest intermolecular distance and correspond to the P–O···H(-C) hydrogen bonds.

3.5. Luminescence

First, the optical properties of the newly synthesized Et_8-PyTPPE were investigated in both solid form and in chloroform ($CHCl_3$), as well as in a 1 wt% poly(methyl methacrylate) (PMMA) polymer film. In chloroform, an absorption spectrum was recorded that showed three distinct bands in the blue (395 nm) and UV ranges (310 nm and 262 nm) (Figure 5, Table 1). The solution had a concentration of 10 mg/L (7.37×10^{-6} mol/L), resulting in a molar absorption coefficient of 52,453 L mol^{-1} cm^{-1} (further absorption coefficients can be found in Table 1).

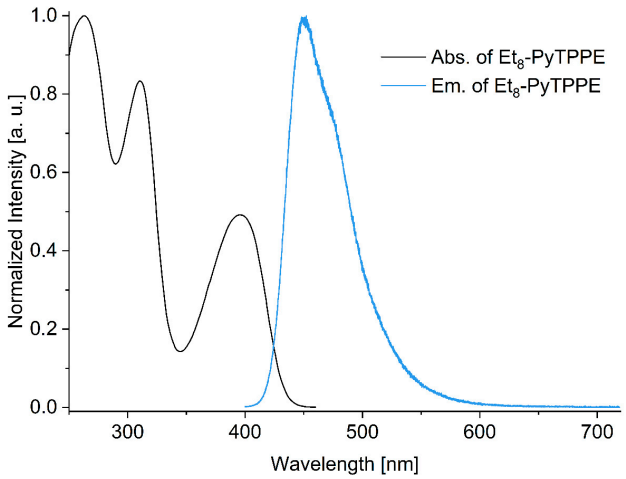

Figure 5. Absorption and emission spectra ($\lambda_{exc.}$ = 375 nm) of Et_8-PyTPPE in $CHCl_3$ at a concentration of 7.37×10^{-6} mol/L.

Steady-state emission measurements show a maximum emission at 452 nm for Et_8-PyTPPE in solution with a weak shoulder at 476 nm (Figure 5). By changing the concentration, we were unable to detect any change in the respective emission bands (Figure S16). Emission measurements under excitation at the respective absorption maxima also do not result in a shift of the emission band, but only in a change in emission intensity (Figure S17). This behavior can be explained by excitation into higher energy electronic states.

Table 1. Spectroscopic parameters of Et_8-PyTPPE at different conditions.

Parameters	$CHCl_3$ Solution	PMMA Film	Solid
1st $\lambda_{abs.\ max}$ [nm]	395	-	-
2nd $\lambda_{abs.\ max}$ [nm]	310	-	-
3rd $\lambda_{abs.\ max}$ [nm]	262	-	-
1st ε_{max} [L mol^{-1} cm^{-1}]	52,453	-	-
2nd ε_{max} [L mol^{-1} cm^{-1}]	88,913	-	-
3rd ε_{max} [L mol^{-1} cm^{-1}]	106,940	-	-
1st $\lambda_{em.\ max}$ [nm] [a]	452	456	480
1st $\lambda_{em.\ shoulder}$ [nm] [a]	476	-	512
2nd $\lambda_{em.\ shoulder}$ [nm] [a]	-	-	550
Stokes shift [nm]	57	-	-
FWHM [nm]	57	61	69
1st $\lambda_{em.\ max}$ [nm] [b]	442	456	482
1st $\lambda_{em.\ shoulder}$ [nm] [b]	462	-	465
2nd $\lambda_{em.\ shoulder}$ [nm] [b]	-	-	512
3rd $\lambda_{em.\ shoulder}$ [nm] [b]	-	-	550
τ_{fl} [ns] [a]	1.5	2.2	1.1
τ_{fl} [ns] [b]	1.4	2	1.1

[a] Measured at 298 K. [b] Measured at 79 K.

Based on the absorption and emission spectra, the 0–0 transition, the Stokes shift, and the full width at half maximum (FWHM) of the emission band could be determined. The 0–0 transition was defined as the intersection of the normalized absorption and emission spectra and lies at a wavelength of 424 nm, corresponding to an energy of 2.92 eV. The respective absorption and emission maxima result in a Stokes shift of 57 nm. The emission band has a FWHM of 57 nm (or 2686.5 cm^{-1}) at 298 K.

In the PMMA polymer film, there is a slight bathochromic shift of the emission maximum by 4 nm to 456 nm compared to the solution. However, no significant change in the FWHM was observed (see Table 1). The emission behavior in the neat solid is significantly different. Et_8-PyTPPE appears yellow in the solid state and exhibits turquoise luminescence under UV excitation (Figure S18). The emission spectrum at 298 K has a maximum at 480 nm, pronounced shoulders at 512 nm, and a weaker shoulder at 550 nm (Figure 6a). Both the shift in the emission maximum and the formation of several shoulders can be attributed to energetic or aggregation phenomena in the solid, which lead to the formation of different luminescent species.

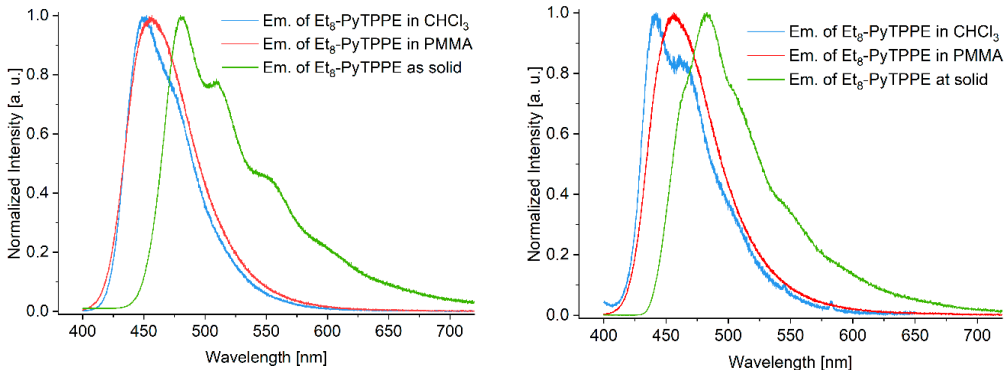

Figure 6. Emission spectra of Et_8-PyTPPE in $CHCl_3$ solution (blue), Et_8-PyTPPE in PMMA polymer film (red), and Et_8-PyTPPE as a solid (green) at (**a**) 298 K and (**b**) at 79 K. $\lambda_{exc.}$ = 375 nm for all spectra.

Cooling to 79 K resulted in significant changes in the emission spectra in both solution and solid (Figure 6b). While the emission maximum of the solution shifts hypsochromically by about 10 nm, the emission maximum of the solid remains almost unchanged. The previously weak shoulder in solution becomes significantly more intense at 79 K and forms a separate maximum at 462 nm. This splitting and shift is well known for organic dyes and can be attributed to reduced molecular dynamics and the altered microscopic environment at low temperatures. In the solid, however, the shoulders observed at 298 K decrease in intensity, while a new shoulder forms at the higher energy side at 465 nm. These changes can be explained by temperature-dependent processes such as the suppression of vibronic relaxations (for a direct overlay and comparison of the spectra at 298 K and 79 K, see Figures S19 and S20).

In contrast, the polymer film shows no change in band shape or emission maximum, suggesting a rigid environment at both 298 K and 79 K. Due to the low loading of 1 wt%, aggregation of the dye is also largely suppressed (overlay in Figure S21).

Lifetime measurements at 298 K and at 79 K yield fluorescence lifetimes in the range of 1–2 ns for all three states (solution, polymer film, and solid). A significant prolongation of the lifetime, which would indicate phosphorescence, could not be detected with the measurement methods used, neither at 298 K nor at 79 K (for lifetime measurements, see Figures S22–S27). It can be seen that the decay curves in both solution and polymer film can be described by a first-order monoexponential fit, both at 298 K and at 79 K. This indicates the presence of a dominant emitting species in each case. In contrast, the time-resolved emission behavior of the solid can only be adequately described by a tri-exponential fit. This result suggests the presence of several luminescent species or different emission centers in the solid, which is consistent with the aggregation effects discussed above.

4. Conclusions

In summary, we presented a modular and synthetically flexible approach to synthesize the phosphonated pyrene compound Et_8-PyTPPE by employing a building block concept that utilizes the formation of C–P and C–B bonds in two separate building blocks. This strategy overcomes the significant limitations of conventional late-stage phosphonation, enabling milder and more economical reaction conditions, as well as improved compatibility of different functional groups. Nickel-catalyzed phosphonation of dibromobiphenyl provides rapid and easy access to a versatile phosphonated intermediate. The complementary borated pyrene building block enables convergent assembly via Suzuki cross-coupling. Both intermediates are broadly applicable synthons for various transition metal-catalyzed coupling reactions. This significantly expands the structural variability of phosphonated aromatic materials.

Single-crystal X-ray diffraction showed that the pyrene skeleton in Et_8-PyTPPE is essentially planar. Yet, the twisting of the biphenylphosphonate arms and the up-and-down orientation of the ethoxy groups at the phosphonate moiety suppress efficient π–π stacking, resulting in a packing motif primarily determined by weak intermolecular interactions. Hirshfeld surface and fingerprint analyses demonstrate that the crystal packing is dominated by H···H and C···H contacts, while O···H interactions with the phosphoryl oxygen atoms represent minor directional contributions. Photophysical studies reveal environment-dependent emission behavior, including structured blue fluorescence in solution and aggregation-influenced, bathochromically shifted emission in the solid state. Nanosecond lifetimes confirm purely fluorescent decays. Together, the safer, tin-free synthesis approach and the structural and optical properties of the synthesized Et_8-PyTPPE could open up interesting possibilities and applications for these phosphonated organic materials. One potential application for our compound is in sensor technology. As already described

by Venkatramaiah et al. [52], various types of explosives can be detected using this class of compounds. In addition to sensors, these compounds could also be used in the manufacture of new OLEDs. Through deprotection, our compound could also be used in the synthesis of new phosphonate-based MOFs or as a coating material in photovoltaic systems.

Supplementary Materials: The following supporting information can be downloaded at: https://www.mdpi.com/article/10.3390/cryst16030196/s1, Reference [82] is cited in the Supplementary Materials.

Author Contributions: Conceptualization, A.L., M.N.A.F. and C.J.; synthesis, M.N.A.F.; methodology, A.L. and M.N.A.F.; software, A.L.; validation, A.L. and M.N.A.F.; formal analysis, A.L. and M.N.A.F.; investigation, A.L. and M.N.A.F.; resources, C.J.; data curation, A.L. and M.N.A.F.; writing—original draft preparation, A.L., M.N.A.F. and C.J.; writing—review and editing, A.L., M.N.A.F. and C.J.; visualization, A.L., M.N.A.F. and C.J.; supervision, C.J.; project administration, C.J.; funding acquisition, C.J. All authors have read and agreed to the published version of the manuscript.

Funding: Funding was provided by Deutsche Forschungsgemeinschaft (DFG), under grant 440366605 (for the Rigaku diffractometer).

Data Availability Statement: The data presented in this study are available upon request from the corresponding author. The CCDC number 2472477 for compound Et_8-PyTPPE contains the supplementary crystallographic data reported in this paper. These data can be obtained free of charge from the Cambridge Crystallographic Data Center via www.ccdc.cam.ac.uk/data_request/cif (accessed on 14 January 2026).

Acknowledgments: The authors would like to thank the Center for Molecular and Structural Analytics at Heinrich Heine University (CeMSA@HHU) for recording the mass spectrometric and NMR spectrometric data.

Conflicts of Interest: The authors declare no conflicts of interest.

References

1. Geng, Z.X.; Wang, Z.T.; Liu, H.L.; Su, X.Y.; Hu, L.Y.; Song, F.Y.; Yao, K. High performance self-assembled pyrene-based emitter with narrowband emission and excellent luminescence efficiency. *RSC Adv.* **2025**, *15*, 25771–25775. [CrossRef]
2. Xing, Y.J.; Xu, X.J.; Zhang, P.; Tian, W.J.; Yu, G.; Lu, P.; Liu, Y.Q.; Zhu, D.B. Carbazole-pyrene-based organic emitters for electroluminescent device. *Chem. Phys. Lett.* **2005**, *408*, 169–173. [CrossRef]
3. Kim, Y.H.; Yoon, D.K.; Lee, E.H.; Ko, Y.K.; Jung, H.T. Photoluminescence properties of a perfluorinated supramolecular columnar liquid crystal with a pyrene core: Effects of the ordering and orientation of the columns. *J. Phys. Chem. B* **2006**, *110*, 20836–20842. [CrossRef]
4. Xia, Z.A.; Yao, M.M.; Wang, S.Y.; Yang, D.J.; Wang, Z.Y.; Wu, R.Y.; Zhang, S.T.; Liu, H.C.; Yang, B. Tailoring pyrene excimer luminescence *via* controlled sulfur oxidation. *J. Mater. Chem. C* **2024**, *12*, 9305–9311. [CrossRef]
5. Figueira-Duarte, T.M.; Mullen, K. Pyrene-based materials for organic electronics. *Chem. Rev.* **2011**, *111*, 7260–7314. [CrossRef]
6. Yang, T.; Cheng, Z.; Li, Z.Q.; Liang, J.X.; Xu, Y.C.; Li, C.L.; Wang, Y. Improving the Efficiency of Red Thermally Activated Delayed Fluorescence Organic Light-Emitting Diode by Rational Isomer Engineering. *Adv. Funct. Mater.* **2020**, *30*, 2002681. [CrossRef]
7. Liu, Y.; Liu, H.; Bai, Q.; Du, C.; Shang, A.; Jiang, D.; Tang, X.; Lu, P. Pyrene[4,5-d]imidazole-Based Derivatives with Hybridized Local and Charge-Transfer State for Highly Efficient Blue and White Organic Light-Emitting Diodes with Low Efficiency Roll-Off. *ACS Appl. Mater. Interfaces* **2020**, *12*, 16715–16725. [CrossRef] [PubMed]
8. Zeng, J.; Qiu, N.L.; Zhang, J.Y.; Wang, X.H.; Redshaw, C.; Feng, X.; Lam, J.W.Y.; Zhao, Z.J.; Tang, B.Z. Y-Shaped Pyrene-Based Aggregation-Induced Emission Blue Emitters for High-Performance OLED Devices. *Adv. Opt. Mater.* **2022**, *10*, 2200917. [CrossRef]
9. Jung, H.; Kang, S.; Lee, H.; Yu, Y.J.; Jeong, J.H.; Song, J.; Jeon, Y.; Park, J. High Efficiency and Long Lifetime of a Fluorescent Blue-Light Emitter Made of a Pyrene Core and Optimized Side Groups. *ACS Appl. Mater. Interfaces* **2018**, *10*, 30022–30028. [CrossRef]
10. Ju, H.J.; Wang, K.; Zhang, J.; Geng, H.; Liu, Z.T.; Zhang, G.X.; Zhao, Y.S.; Zhang, D.Q. 1,6-and 2,7-*trans*-β-Styryl Substituted Pyrenes Exhibiting Both Emissive and Semiconducting Properties in the Solid State. *Chem. Mater.* **2017**, *29*, 3580–3588. [CrossRef]
11. Hai, X.; Fang, L.; Xiong, M.; Zhou, X.; Wang, S.; Sun, H.; Su, C.; Chen, H. Charge Density Modulation of Pyrene-Related Small Molecules by Nitrogen Heteroatoms Precisely Regulates Photocatalytic Generation of Hydrogen. *ACS Nano* **2023**, *17*, 20570–20579. [CrossRef]

12. Han, C.Z.; Dong, P.H.; Tang, H.R.; Zheng, P.Y.; Zhang, C.; Wang, F.; Huang, F.; Jiang, J.X. Realizing high hydrogen evolution activity under visible light using narrow band gap organic photocatalysts. *Chem. Sci.* **2021**, *12*, 1796–1802. [CrossRef] [PubMed]
13. Xiang, S.H.; Han, C.Z.; Shu, C.; Zhang, C.; Jiang, J.X. Structure evolution of thiophene-containing conjugated polymer photocatalysts for high-efficiency photocatalytic hydrogen production. *Sci. China Mater.* **2022**, *65*, 422–430. [CrossRef]
14. Shu, C.; Han, C.; Yang, X.; Zhang, C.; Chen, Y.; Ren, S.; Wang, F.; Huang, F.; Jiang, J.X. Boosting the Photocatalytic Hydrogen Evolution Activity for D-pi-A Conjugated Microporous Polymers by Statistical Copolymerization. *Adv. Mater.* **2021**, *33*, e2008498. [CrossRef]
15. Kosugi, K.; Akatsuka, C.; Iwami, H.; Kondo, M.; Masaoka, S. Iron-Complex-Based Supramolecular Framework Catalyst for Visible-Light-Driven CO_2 Reduction. *J. Am. Chem. Soc.* **2023**, *145*, 10451–10457. [CrossRef]
16. Nasrallah, H.; Lyu, P.B.; Maurin, G.; El-Roz, M. Highly efficient CO_2 reduction under visible-light on non-covalent Ru···Re assembled photocatalyst: Evidence on the electron transfer mechanism. *J. Catal.* **2021**, *404*, 46–55. [CrossRef]
17. Zhao, S.; Li, N.J.; Xu, Q.F.; Li, H.; Lu, J.M.; Chen, D.Y. Grafting small organic molecules on donor-acceptor polymers to regulate electron push-pull interactions for efficient H_2O_2 production. *Chem. Eng. J.* **2024**, *488*, 150813. [CrossRef]
18. Luo, Z.; Chen, X.; Hu, Y.; Chen, X.; Lin, W.; Wu, X.; Wang, X. Side-Chain Molecular Engineering of Triazole-Based Donor-Acceptor Polymeric Photocatalysts with Strong Electron Push-Pull Interactions. *Angew. Chem. Int. Ed.* **2023**, *62*, e202304875. [CrossRef]
19. Zhang, Y.N.; Yang, X.; Tang, H.D.; Liang, D.; Wu, J.; Huang, D.J. Pyrenediones as versatile photocatalysts for oxygenation reactions with *in situ* generation of hydrogen peroxide under visible light. *Green Chem.* **2020**, *22*, 22–27. [CrossRef]
20. Watanabe, H.; Nakajima, K.; Ekuni, K.; Edagawa, R.; Akagi, Y.; Okuda, Y.; Wakamatsu, K.; Orita, A. Custom-Made Pyrene Photocatalyst-Promoted Desulfonylation of Arylethenyl Sulfones Using Green-Light-Emitting Diodes. *Synthesis* **2021**, *53*, 2984–2994. [CrossRef]
21. Manandhar, E.; Wallace, K.J. Host-guest chemistry of pyrene-based molecular receptors. *Inorg. Chim. Acta* **2012**, *381*, 15–43. [CrossRef]
22. Hung, H.C.; Cheng, C.W.; Ho, I.T.; Chung, W.S. Dual-mode recognition of transition metal ions by bis-triazoles chained pyrenes. *Tetrahedron Lett.* **2009**, *50*, 302–305. [CrossRef]
23. Zhou, Y.; Zhu, C.Y.; Gao, X.S.; You, X.Y.; Yao, C. Hg^{2+}-selective ratiometric and "off-on" chemosensor based on the azadiene-pyrene derivative. *Org. Lett.* **2010**, *12*, 2566–2569. [CrossRef] [PubMed]
24. Wang, F.; Nandhakumar, R.; Moon, J.H.; Kim, K.M.; Lee, J.Y.; Yoon, J. Ratiometric Fluorescent Chemosensor for Silver Ion at Physiological pH. *Inorg. Chem.* **2011**, *50*, 2240–2245. [CrossRef]
25. Laschuk, N.O.; Ebralidze, I.I.; Spasyuk, D.; Zenkina, O.V. Multi-Readout Logic Gate for the Selective Detection of Metal Ions at the Parts Per Billion Level. *Eur. J. Inorg. Chem.* **2016**, *2016*, 3530–3535. [CrossRef]
26. Wakchaure, V.C.; Ranjeesh, K.C.; Goudappagouda, G.; Das, T.; Vanka, K.; Gonnade, R.; Babu, S.S. Mechano-responsive room temperature luminescence variations of boron conjugated pyrene in air. *Chem. Commun.* **2018**, *54*, 6028–6031. [CrossRef]
27. Pietsch, C.; Vollrath, A.; Hoogenboom, R.; Schubert, U.S. A fluorescent thermometer based on a pyrene-labeled thermoresponsive polymer. *Sensors* **2010**, *10*, 7979–7990. [CrossRef]
28. Gladysiak, A.; Nguyen, T.N.; Bounds, R.; Zacharia, A.; Itskos, G.; Reimer, J.A.; Stylianou, K.C. Temperature-dependent interchromophoric interaction in a fluorescent pyrene-based metal-organic framework. *Chem. Sci.* **2019**, *10*, 6140–6148. [CrossRef]
29. Gong, Y.B.; Zhang, P.; Gu, Y.R.; Wang, J.Q.; Han, M.M.; Chen, C.; Zhan, X.J.; Xie, Z.L.; Zou, B.; Peng, Q.; et al. The Influence of Molecular Packing on the Emissive Behavior of Pyrene Derivatives: Mechanoluminescence and Mechanochromism. *Adv. Opt. Mater.* **2018**, *6*, 1800198. [CrossRef]
30. Yang, J.; Li, L.; Yu, Y.; Ren, Z.C.; Peng, Q.; Ye, S.H.; Li, Q.Q.; Li, Z. Blue pyrene-based AIEgens: Inhibited intermolecular π-π stacking through the introduction of substituents with controllable intramolecular conjugation, and high external quantum efficiencies up to 3.46% in non- doped OLEDs. *Mater. Chem. Front.* **2017**, *1*, 91–99. [CrossRef]
31. Rieth, A.J.; Wright, A.M.; Dinca, M. Kinetic stability of metal-organic frameworks for corrosive and coordinating gas capture. *Nat. Rev. Mater.* **2019**, *4*, 708–725. [CrossRef]
32. Ding, M.; Cai, X.; Jiang, H.L. Improving MOF stability: Approaches and applications. *Chem. Sci.* **2019**, *10*, 10209–10230. [CrossRef] [PubMed]
33. Huang, Y.L.; Ping, L.J.; Wu, J.; Li, Y.Y.; Zhou, X.P. Increasing the Stability of Metal-Organic Frameworks by Coating with Poly(tetrafluoroethylene). *Inorg. Chem.* **2022**, *61*, 5092–5098. [CrossRef]
34. Chen, L.F.; Zhang, B.Y.; Chen, L.L.; Liu, H.N.; Hu, Y.Q.; Qiao, S.L. Hydrogen-bonded organic frameworks: Design, applications, and prospects. *Mater. Adv.* **2022**, *3*, 3680–3708. [CrossRef]
35. Sahoo, R.; Tedy, A.M.; Manna, A.K.; Das, M.C. A Water-Stable Hydrogen-Bonded Organic Framework (HOF) for Selective Sensing of Antibiotics in Aqueous Medium. *Chem. Eur. J.* **2025**, *31*, e202404756. [CrossRef]
36. Evans, A.M.; Ryder, M.R.; Ji, W.; Strauss, M.J.; Corcos, A.R.; Vitaku, E.; Flanders, N.C.; Bisbey, R.P.; Dichtel, W.R. Trends in the thermal stability of two-dimensional covalent organic frameworks. *Faraday Discuss.* **2021**, *225*, 226–240. [CrossRef]

37. Guan, X.; Fang, Q.; Yan, Y.; Qiu, S. Functional Regulation and Stability Engineering of Three-Dimensional Covalent Organic Frameworks. *Acc. Chem. Res.* **2022**, *55*, 1912–1927. [CrossRef]
38. Jia, C.; Liang, R.R.; Gan, S.X.; Jiang, S.Y.; Qi, Q.Y.; Zhao, X. Boosting Hydrostability and Carbon Dioxide Capture of Boroxine-Linked Covalent Organic Frameworks by One-Pot Oligoamine Modification. *Chem. Eur. J.* **2023**, *29*, e202300186. [CrossRef] [PubMed]
39. Mateo, D.; Santiago-Portillo, A.; Albero, J.; Navalón, S.; Alvaro, M.; García, H. Long-Term Photostability in Terephthalate Metal-Organic Frameworks. *Angew. Chem. Int. Ed.* **2019**, *58*, 17843–17848. [CrossRef]
40. Mayeuski, A.V.; Poloneeva, D.Y.; Toshcheva, E.A.; Bardakova, A.V.; Shuruhina, A.V.; Emeline, A.V.; Bahnemann, D.W. UV-induced alteration of luminescence chromaticity of Ln-based MOF-76. *J. Lumin.* **2021**, *235*, 117970. [CrossRef]
41. Gupta, N.K.; Bae, J.; Kim, S.; Kim, K.S. Terephthalate and trimesate metal-organic frameworks of Mn, Co, and Ni: Exploring photostability by spectroscopy. *RSC Adv.* **2021**, *11*, 8951–8962. [CrossRef] [PubMed]
42. Braid, J.L.; Koldemir, U.; Sellinger, A.; Collins, R.T.; Furtak, T.E.; Olson, D.C. Conjugated phosphonic acid modified zinc oxide electron transport layers for improved performance in organic solar cells. *ACS Appl. Mater. Interfaces* **2014**, *6*, 19229–19234. [CrossRef]
43. Bhattacharya, A.K.; Thyagarajan, G. The Michaelis-Arbuzov rearrangement. *Chem. Rev.* **1981**, *81*, 415–430. [CrossRef]
44. Zabri, H.; Odobel, F.; Altobello, S.; Caramori, S.; Bignozzi, C.A. Efficient osmium sensitizers containing 2,2′-bipyridine-4,4′-bisphosphonic acid ligand. *J. Photochem. Photobiol. A Chem.* **2004**, *166*, 99–106. [CrossRef]
45. Owsianik, K.; Romaniuk, A.; Turek, M.; Balczewski, P. Comprehensive Review of Synthesis, Optical Properties and Applications of Heteroarylphosphonates and Their Derivatives. *Molecules* **2024**, *29*, 3691. [CrossRef]
46. Ferrer, I.; Fontrodona, X.; Roig, A.; Rodriguez, M.; Romero, I. A Recoverable Ruthenium Aqua Complex Supported on Silica Particles: An Efficient Epoxidation Catalyst. *Chem. Eur. J.* **2017**, *23*, 4096–4107. [CrossRef] [PubMed]
47. Ashford, D.L.; Song, W.; Concepcion, J.J.; Glasson, C.R.; Brennaman, M.K.; Norris, M.R.; Fang, Z.; Templeton, J.L.; Meyer, T.J. Photoinduced electron transfer in a chromophore-catalyst assembly anchored to TiO_2. *J. Am. Chem. Soc.* **2012**, *134*, 19189–19198. [CrossRef]
48. Chen, B.; Zhao, L.; Ding, J.Q.; Wang, L.X.; Jing, X.B.; Wang, F.S. An alcohol-soluble and ion-free electron transporting material functionalized with phosphonate groups for solution-processed multilayer PLEDs. *Chem. Commun.* **2016**, *52*, 12052–12055. [CrossRef] [PubMed]
49. Li, X.F.; Yang, L.Q.; Wang, C.X.; Wang, S.M.; Ding, J.Q. Bulky Passivation by an Electroactive Phosphonate Dendrimer for High-Performance Perovskite Quantum Dot Light-Emitting Diodes. *J. Phys. Chem. C* **2024**, *128*, 877–884. [CrossRef]
50. Villemin, E.; Elias, B.; Devillers, M.; Marchand-Brynaert, J. A pyrene- and phosphonate-containing fluorescent probe as guest molecule in a host polymer matrix. *Molecules* **2013**, *18*, 1897–1915. [CrossRef]
51. Lewkowski, J.; Rodriguez Moya, M.; Wrona-Piotrowicz, A.; Zakrzewski, J.; Kontek, R.; Gajek, G. Synthesis, fluorescence properties and the promising cytotoxicity of pyrene-derived aminophosphonates. *Beilstein J. Org. Chem.* **2016**, *12*, 1229–1235. [CrossRef]
52. Venkatramaiah, N.; Firmino, A.D.; Almeida Paz, F.A.; Tome, J.P. Fast detection of nitroaromatics using phosphonate pyrene motifs as dual chemosensors. *Chem. Commun.* **2014**, *50*, 9683–9686. [CrossRef] [PubMed]
53. Serrano-Nieto, R.; Carrasco, S.; Morales-Cámara, S.; Rodríguez-Diéguez, A.; Biglione, C.; Salcedo-Abraira, P.; Pérez, Y.; Rojas, S.; Horcajada, P. Novel pyrene phosphonate metal-organic frameworks to efficiently degrade sulfamethazine in wastewater. *J. Environ. Chem. Eng.* **2025**, *13*, 115647. [CrossRef]
54. Firmino, A.D.G.; Mendes, R.F.; Ananias, D.; Figueira, F.; Tomé, J.P.C.; Rocha, J.; Paz, F.A.A. Pyrene Tetraphosphonate-Based Metal-Organic Framework: Structure and Photoluminescence. *Eur. J. Inorg. Chem.* **2020**, *2020*, 3565–3572. [CrossRef]
55. Taylor, J.M.; Vaidhyanathan, R.; Iremonger, S.S.; Shimizu, G.K. Enhancing water stability of metal-organic frameworks via phosphonate monoester linkers. *J. Am. Chem. Soc.* **2012**, *134*, 14338–14340. [CrossRef] [PubMed]
56. Salcedo-Abraira, P.; Biglione, C.; Vilela, S.M.F.; Grape, E.S.; Ureña, N.; Salles, F.; Pérez-Prior, M.T.; Willhammar, T.; Trens, P.; Várez, A.; et al. High Proton Conductivity of a Bismuth Phosphonate Metal-Organic Framework with Unusual Topology. *Chem. Mater.* **2023**, *35*, 4329–4337. [CrossRef]
57. Salcedo-Abraira, P.; Serrano-Nieto, R.; Biglione, C.; Cabrero-Antonino, M.; Vilela, S.M.F.; Babaryk, A.A.; Tilve-Martínez, D.; Rodriguez-Diéguez, A.; Navalón, S.; García, H.; et al. Two Cu-Based Phosphonate Metal–Organic Frameworks as Efficient Water-Splitting Photocatalysts. *Chem. Mater.* **2023**, *35*, 4211–4219. [CrossRef]
58. Schütrumpf, A.; Duthie, A.; Lork, E.; Yücesan, G.; Beckmann, J. Synthesis of Some Di- and Tetraphosphonic Acids by Suzuki Cross-Coupling. *Z. Anorg. Allg. Chem.* **2018**, *644*, 1134–1142. [CrossRef]
59. CrysAlisPro. *Rigaku Oxford Diffraction*, Release 1.171.40.103a; Agilent; Agilent Technologies Ltd.: Yarnton, UK, 2014.
60. Dolomanov, O.V.; Bourhis, L.J.; Gildea, R.J.; Howard, J.A.K.; Puschmann, H. OLEX2: A complete structure solution, refinement and analysis program. *J. Appl. Crystallogr.* **2009**, *42*, 339–341. [CrossRef]
61. Sheldrick, G.M. SHELXT—Integrated space-group and crystal-structure determination. *Acta Crystallogr. A* **2015**, *71*, 3–8. [CrossRef]

62. Sheldrick, G.M. Crystal structure refinement with SHELXL. *Acta Crystallogr. C* **2015**, *71*, 3–8. [CrossRef]
63. Brandenburg, K.; Putz, H. *Diamond Crystal and Molecular Structure Visualization*, Version 5; Crystal Impact Gbr: Bonn, Germany, 2023.
64. Unikela, K.S.; Roemmele, T.L.; Houska, V.; McGrath, K.E.; Tobin, D.M.; Dawe, L.N.; Boeré, R.T.; Bodwell, G.J. Gram-Scale Synthesis and Highly Regioselective Bromination of 1,1,9,9-Tetramethyl[9](2,11)teropyrenophane. *Angew. Chem. Int. Ed.* **2018**, *57*, 1707–1711. [CrossRef]
65. Zhang, Y.Y.; Nong, J.L.; Wang, Y.X. Visible-light promoted late-stage chlorination and bromination of quinones and (hetero)arenes utilizing aqueous HCl or HBr as halogen donors. *Commun. Chem.* **2025**, *9*, 23. [CrossRef]
66. Tan, Z.; Liu, Y.; Helmy, R.; Rivera, N.R.; Hesk, D.; Tyagarajan, S.; Yang, L.; Su, J. Electrochemical bromination of late stage intermediates and drug molecules. *Tetrahedron Lett.* **2017**, *58*, 3014–3018. [CrossRef]
67. Khan, A.H.; Chen, J.S. Synthesis of Breitfussin B by Late-Stage Bromination. *Org. Lett.* **2015**, *17*, 3718–3721. [CrossRef]
68. Maares, M.; Ayhan, M.M.; Yu, K.B.; Yazaydin, A.O.; Harmandar, K.; Haase, H.; Beckmann, J.; Zorlu, Y.; Yucesan, G. Alkali Phosphonate Metal-Organic Frameworks. *Chem. Eur. J.* **2019**, *25*, 11214–11217. [CrossRef]
69. Schütrumpf, A.; Kirpi, E.; Bulut, A.; Morel, F.L.; Ranocchiari, M.; Lork, E.; Zorlu, Y.; Grabowsky, S.; Yücesan, G.; Beckmann, J. Tetrahedral Tetraphosphonic Acids. New Building Blocks in Supramolecular Chemistry. *Cryst. Growth Des.* **2015**, *15*, 4925–4931. [CrossRef]
70. Bulut, A.; Zorlu, Y.; Wörle, M.; Pasa, S.; Kurt, H.; Zubieta, J.; Beckmann, J.; Yücesan, G. Rational Design of Two-Dimensional Bimetallic Wave Structures from Zigzag Chains via Site-Specific Coordination around the 2,6-Naphthalenediphosphonic Acid Motif. *Eur. J. Inorg. Chem.* **2016**, *2016*, 3506–3512. [CrossRef]
71. Janiak, C. A Critical Account on π–π Stacking in Metal Complexes with Aromatic Nitrogen-Containing Ligands. *J. Chem. Soc. Dalton Trans.* **2000**, *21*, 3885–3896. [CrossRef]
72. Yang, X.-J.; Drepper, F.; Wu, B.; Sun, W.-H.; Haehnel, W.; Janiak, C. From Model Compounds to Protein Binding: Syntheses, Characterizations and Fluorescence Studies of $[Ru^{II}$ (Bipy)(Terpy)L$]^{2+}$ Complexes (Bipy = 2,2′-Bipyridine; Terpy = 2,2′:6′,2″-Terpyridine; L = Imidazole, Pyrazole and Derivatives, Cytochrome c). *Dalton Trans.* **2005**, *2*, 256–267. [CrossRef]
73. Takahashi, O.; Kohno, Y.; Iwasaki, S.; Saito, K.; Iwaoka, M.; Tomoda, S.; Umezawa, Y.; Tsuboyama, S.; Nishio, M. Hydrogen-Bond-Like Nature of the CH/π Interaction as Evidenced by Crystallographic Database Analyses and Ab Initio Molecular Orbital Calculations. *Bull. Chem. Soc. Jpn.* **2001**, *74*, 2421–2430. [CrossRef]
74. Nishio, M.; Umezawa, Y.; Honda, K.; Tsuboyama, S.; Suezawa, H. CH/π Hydrogen Bonds in Organic and Organometallic Chemistry. *CrystEngComm* **2009**, *11*, 1757–1788. [CrossRef]
75. Macrae, C.F.; Sovago, I.; Cottrell, S.J.; Galek, P.T.A.; McCabe, P.; Pidcock, E.; Platings, M.; Shields, G.P.; Stevens, J.S.; Towler, M.; et al. *Mercury 4.0*: From visualization to analysis, design and prediction. *J. Appl. Crystallogr.* **2020**, *53*, 226–235. [CrossRef]
76. Venkatramaiah, N.; Pereira, C.F.; Mendes, R.F.; Paz, F.A.A.; Tomé, J.P.C. Phosphonate Appended Porphyrins as Versatile Chemosensors for Selective Detection of Trinitrotoluene. *Anal. Chem.* **2015**, *87*, 4515–4522. [CrossRef]
77. Zheng, T.; Yang, Z.; Gui, D.; Liu, Z.; Wang, X.; Dai, X.; Liu, S.; Zhang, L.; Gao, Y.; Chen, L.; et al. Overcoming the crystallization and designability issues in the ultrastable zirconium phosphonate framework system. *Nat. Commun.* **2017**, *8*, 15369. [CrossRef]
78. Spackman, P.R.; Turner, M.J.; McKinnon, J.J.; Wolff, S.K.; Grimwood, D.J.; Jayatilaka, D.; Spackman, M.A. CrystalExplorer: A program for Hirshfeld surface analysis, visualization and qu antitative analysis of molecular crystals. *J. Appl. Cryst.* **2021**, *54*, 1006–1011. [CrossRef] [PubMed]
79. Castro, J.; Ferraro, V.; Bortoluzzi, M. Single-Crystal X-ray Structure Determination of Tris(pyrazol-1-yl)methane Triphenylphosphine Copper(I) Tetrafluoroborate, Hirshfeld Surface Analysis and DFT Calculations. *Crystals* **2024**, *14*, 162. [CrossRef]
80. Mohabbat, A.; Boldog, I.; Sohi, T.H.H.; Reistel, N.; Seiffert, P.; Janiak, C. Hydrogen-Bonded Ladder Motifs in Naphthalene Dicarboxamides: Influence of Linear vs. Angular Amide Orientation. *Crystals* **2025**, *15*, 406. [CrossRef]
81. El Hafi, M.; Anouar, E.H.; Lahmidi, S.; Boulhaoua, M.; Loubidi, M.; Alanazi, A.S.; Filali, I.; Hefnawy, M.; El Ghayati, L.; Mague, J.T.; et al. Synthesis of New Pyrazolo[3,4-*d*]pyrimidine Derivatives: NMR Spectroscopic Characterization, X-Ray, Hirshfeld Surface Analysis, DFT, Molecular Docking, and Antiproliferative Activity Investigations. *Molecules* **2024**, *29*, 5020. [CrossRef]
82. Subianto, S.; Choudhury, N.R.; Dutta, N.K. Palladium-Catalyzed Phosphonation of SEBS Block Copolymer. *J. Polym. Sci. A Polym. Chem.* **2008**, *46*, 5431–5441. [CrossRef]